Optics Communications 501 (2021) 127341

Contents lists available at ScienceDirect

Optics Communications

journal homepage: www.elsevier.com/locate/optcom

REM: A simplified revised entropy image reconstruction for photonics integrated interference imaging system

TianBao Chen [a,b], XueFeng Zeng [a,*], ZhiYu Zhang [a], Feng Zhang [a,*], YingYing Bai [a,b], XueJun Zhang [a]

[a] Key Laboratory of Optical System Advanced Manufacturing Technology, Changchun Institute of Optics, Fine Mechanics and Physics, Chinese Academy of Sciences, Changchun 130033, China

[b] University of Chinese Academy of Sciences, Beijing 100049, China

ARTICLE INFO

Keywords:
Photonics integrated interference imaging system
Gibbs-ringing artifacts
Entropy
Image reconstruction

ABSTRACT

The photonics integrated interference imaging system (PIIIS) is a recently developed far-field imaging approach aimed at compacting structures and acquiring high imaging performance. In this regard, to acquire higher imaging quality, several lens patterns have been developed, providing low-frequency intensive but high-frequency sparse measurements of the visibility function. However, sparse measurements at high frequency produce Gibbs-ringing artifacts in the image reconstruction, severely damaging the PIIIS imaging quality. In this study, a new data penalty for revised entropy is proposed for PIIIS, and a simple reconstruction algorithm using the Newton method is developed. A reconstruction experiment adopting the hierarchical multistage pattern is implemented on resolution board (USAF1951) targets with bright and black backgrounds. The outstanding improvement in the experimental results proves the feasibility of suppressing the ringing artifacts in the images reconstructed in PIIIS.

1. Introduction

The spatial resolution of conventional diffraction-limited optical systems is proportional to the diameter of the pupil. Currently, higher spatial resolution is required for human activities and research, leading to a dramatic increase in the size, weight, and power (SWaP) of the conventional optical systems. A new imaging telescope, the Segmented Planar Imaging Detector for Electro-optical Reconnaissance (SPIDER), has been proposed based on standard imaging interferometer techniques [1,2]. The SPIDER imager can reduce SWaP by ~10–100 times for a similar resolution by introducing photonic integrated circuits (PICs) and replacing bulk lens systems with compact lenslets array [3]. Hence, the SPIDER imager comprises two parts: a sensor system and a signal-processing module. The sensor system consists of a lenslet array and couples spatial light into a signal-processing module. The signal-processing module is used to obtain four balanced four-quadrature interference signals and contains waveguide arrays, arrayed waveguide gratings (AWGs), and balanced four-quadrature detectors (BFQDs) [4–6]. Subsequently, these detected photocurrent signals can be used to calculate complex visibility by digital signal processing.

The SPIDER imager interferes with the light from two different lenslets spaced apart by a distance vector $\vec{B}$, also called the baseline. The separate two lenslets produce an angular resolution inversely proportional to B and independent of the individual telescope diameter. Based on the Van Cittert–Zernike theorem, interference signal measures the certain complex visibility corresponding to spatial frequency $\vec{f} = \vec{B}/\lambda z$, where λ is the observing wavelength and z is the distance from the target to the imager pupil plane. Subsequently, the visibilities are arranged in a numerical matrix considering the spatial frequency as the coordinate [3]. To some extent, the complex visibility matrix corresponds to the Fourier transform of observation. Hence, by applying the inverse Fourier transform (IFT) to the visibility matrix, the observed targets can be reconstructed. Moreover, the image quality is mainly related to acquiring the visibilities filled in the matrix of different spatial frequencies.

To improve imaging quality, several lenslet array patterns have been proposed for the photonics integrated interference imaging system (PIIIS), such as SPIDER pairing methods [5], hierarchical multistage pattern [6], rectangular pattern [7], and hexagonal array pattern [8]. Chu et al. [5] proposed an adjustable baseline pairing method to acquire better imaging quality for different frequency-intensive targets. For natural scenes, they are low-frequency intensive targets, characterized by a heavy-tailed gradient distribution [9]. Hence, low-frequency intensive patterns tend to acquire higher imaging quality. The subsequent patterns focus on filling the low-frequency complex visibilities and they ingeniously propose observing the zero-frequency visibility [6–8], improving imaging quality.

* Corresponding authors.
E-mail addresses: zxf@ciomp.ac.cn (X. Zeng), zhangfjyz@sina.cn (F. Zhang).

https://doi.org/10.1016/j.optcom.2021.127341
Received 15 June 2021; Received in revised form 27 July 2021; Accepted 1 August 2021
Available online 5 August 2021

The imaging improvements using the low-frequency intensive pairing method have been confirmed for most observations. For some special observations, which are high/middle-frequency intensive, adjustable pairing methods could guarantee image quality [5]. All pairing patterns lead to sparse sampling in some "unimportant" frequencies, and adding sampling for these "unimportant" frequencies would be expensive. However, Gibbs-ringing artifacts are produced when reconstructing images raised by sparse sampling [10,11]. Moreover, PIIIS is more capable of observing targets with significant gradient changes, which can be explained through compressive sampling [8,12]. However, targets with significant gradient changes further aggravate the Gibbs-ringing artifacts, and these artifacts severely reduce the imaging quality of PIIIS.

Currently, several approaches have been proposed to reduce the disturbances due to Gibbs-ringing artifacts in Magnetic resonance imaging [13]. One of the more direct methods is image filtering. However, this method leads to blurring and a significant reduction of high-frequency information [14]. Based on Gegenbauer polynomials, more advanced algorithms have been proposed for reconstructing smooth areas piecewise [15]. Nevertheless, the requirements for precise edge detection are still a challenge for degraded images. Deep learning techniques, especially convolutional neural networks, have been applied to suppress ringing artifacts [13]. However, the reliability of the training images depends greatly on the available databases. Moreover, PIIIS is used for far-field imaging, and thus it is difficult to obtain the brightness distribution of observation.

Several outstanding image reconstruction algorithms have been proposed for radio/optical interferometer, such as maximum entropy methods (MEM) [16]. The underlying idea of MEM is to obtain the least informative image that is consistent with the data. Inspired by the well-developed entropy method in optical interferometry, we propose a prior image based penalty designed to preserve the advantage of entropy and stabilize the algorithm. Hence, the data penalty term is termed "revised entropy". The penalty is designed to penalize high bias deviating from the ringing-free or ringing-less prior images. Moreover, the data penalty term of this method has a "U-shape" design, which is typical of convex functions. When minimizing this "U-shaped term" with the L2 data fidelity norm, the reconstruction drops to the prior, set as the bottom of the U-shaped term, and simultaneously maintains data fidelity.

To demonstrate the reconstruction of the revised entropy for PIIIS, we developed a simple revised entropy algorithm using the Newton method and adopted a hierarchical multistage pattern as the image reconstruction system architecture [6]. In addition to the revised entropy penalty, other restrictions are also added to the revised entropy algorithm to obtain reconstruction images.

The remainder of this paper is structured as follows. In Section 2, we briefly describe the forward imaging model mathematically and present the overall structure of the PIIIS. In Section 3, the entropy is presented. Subsequently, we introduce the revised entropy penalty and develop a simple revised entropy algorithm using the Newton method. In Section 4, we demonstrate the feasibility of suppressing ringing artifacts using bright and black background resolution board (USAF1951) targets. The conclusions are presented in Section 5.

2. Imaging principles

For incoherent extended observations in the far-field, the Van Cittert–Zernike theory provides the complex visibility of two different points in the uv plane, namely the lenslet array plane [2] as follows:

$$V\left(\vec{D}_1,\vec{D}_2,\lambda\right)=\int_{\Sigma}\mathrm{I}^0\left(\vec{x}\right)\exp\left\{-2\frac{\mathrm{i}\pi}{\lambda z_0}\left[\left(\vec{D}_1-\vec{D}_2\right)\bullet\vec{x}\right]\right\}\mathrm{d}\vec{x} \tag{1}$$

where $\vec{D}_1$ and $\vec{D}_2$ are coordinate vectors of two lenslets in the uv plane, $\vec{x}$ is the coordinate vector for the observation plane, and z_0 represents the distance between the two planes. $\mathrm{I}^0(\vec{x})$ is the brightness distribution of the observation and $\vec{B}=\vec{D}_1-\vec{D}_2$ is the baseline vector. The spatial frequency can be expressed as follows:

$$\vec{f}=(\mu,\nu)=\frac{\vec{B}}{\lambda z_0} \tag{2}$$

PICs are introduced to calculate the complex visibilities of different spatial frequencies. A diagram of a PIIIS is shown in Fig. 1. A pair of lenslets composes one baseline, and each lenslet is equipped with n input waveguides to obtain an approximately $2n\lambda/D$ field of view (FOV) [17]. The AWGs and BFQDs are used to obtain four-quadrature signals of quasi-monochromatic light λ with a baseline $\vec{B}$ [3]. The complex visibility is solved using the quadrature modulation detection technique [5,6].

The visibility function V is hidden in four-quadrature signals $\mathrm{I_A}$, $\mathrm{I_B}$, $\mathrm{I_C}$, $\mathrm{I_D}$ as follows:

$$\begin{aligned}
\mathrm{I_A}&=\frac{1}{4}\left(\mathrm{I_1}+\mathrm{I_2}+2\sqrt{\mathrm{I_1I_2}}\,|V|\cos\varphi\right)\\
\mathrm{I_B}&=\frac{1}{4}\left(\mathrm{I_1}+\mathrm{I_2}+2\sqrt{\mathrm{I_1I_2}}\,|V|\sin\varphi\right)\\
\mathrm{I_C}&=\frac{1}{4}\left(\mathrm{I_1}+\mathrm{I_2}-2\sqrt{\mathrm{I_1I_2}}\,|V|\cos\varphi\right)\\
\mathrm{I_D}&=\frac{1}{4}\left(\mathrm{I_1}+\mathrm{I_2}-2\sqrt{\mathrm{I_1I_2}}\,|V|\sin\varphi\right)
\end{aligned} \tag{3}$$

The complex visibility $V=|V|e^{i\varphi}$, including amplitude $|V|$ and phase φ, is then obtained as follows:

$$|V|^2=\frac{\left(\mathrm{I_A}-\mathrm{I_C}\right)^2+\left(\mathrm{I_B}-\mathrm{I_D}\right)^2}{\mathrm{I_1I_2}} \tag{4}$$

$$\varphi=\mathrm{arctg}\left(\frac{\mathrm{I_B}-\mathrm{I_D}}{\mathrm{I_A}-\mathrm{I_C}}\right) \tag{5}$$

The complex visibilities matrix of the brightness distribution of various nonredundant spatial frequencies $\vec{f}$ can be established.

3. Reconstruction algorithm

3.1. The revised entropy penalty

The MEM algorithm achieved great success in astronomical observations [16,18]. Among the infinite number of possible images that agree with the visibility measurements, the MEM is designed to select the image containing the least amount of information, and thus the least amount of false information [18,19], such as Gibbs-ringing artifacts. The information entropy is given as follows:

$$\mathrm{E}=-\sum_{\mathrm{j}}^{\mathrm{N}}\mathrm{I_j}\ln(\mathrm{I_j}/\mathrm{M_j}) \tag{6}$$

where $\mathrm{I_j}$ is a discrete representation of the images in position j and $\mathrm{M_j}$ is the default model image allowing the incorporation of prior information regarding the observations.

Based on entropy, we propose $\mathrm{M_j}$ that could operate as a prior image to suppress ringing artifacts. The prior image can be set as ringing-free or ringing-less and used to penalize a high bias deviating from it. So, this penalty term should have a "U-shape", which is typical of a convex function. When minimizing this "U-shaped" term with the L2 data fidelity norm [20], the reconstructed image drops to the prior, which is set as the inflection point of the "U-shaped" term, retaining data fidelity. To preserve the advantage of information entropy and stabilize the iterations without a sophisticated scheme, we propose the revised entropy given as follows:

$$\mathrm{H}=-\sum_{\mathrm{j}}^{\mathrm{N}}\mathrm{I_j}\exp(-\mathrm{I_j}/\mathrm{I_p}) \tag{7}$$

This term allows restoration $\mathrm{I_j}$ close to zero and dampens a high deviation from prior intensity $\mathrm{I_p}$. The prior $\mathrm{I_p}$ can have different alternatives, such as a uniform matrix with the same value or a filtering image:

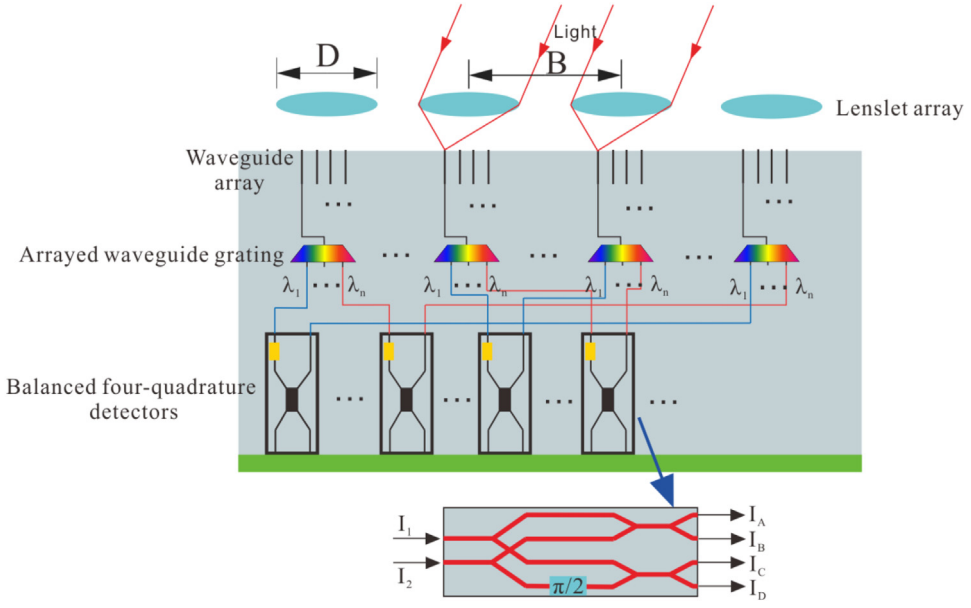

Fig. 1. Structure diagram of the photonics integrated interference imaging system (PIIIS).

(1) For a uniform matrix, the value is suggested as the average energy of the brightness distribution, which can be obtained through the visibility of zero-frequency owing to Parseval's theorem [21].
(2) For a filtering image, different filtering methods (e.g., Gaussian or Lanczos) can be used [10,14]. One of these filters is added to the visibility matrix before IFT, which is equivalent to windowed IFT.

However, H is found to be not convex in the nonnegative real numbers domain $\boldsymbol{R}_+$, which leads to instability and difficulty in iterations using gradient descent optimization algorithms. It is noticed that H is convex on $[0, 2I_p]$ and is non-convex on $(2I_p, +\infty)$. Nevertheless, certain techniques can be added for the optimization:

(1) The initial estimations I_j are set to near zero and $I_j \subset \boldsymbol{R}_+$.
(2) The revised entropy can be modified as $H = -\sum_j^N I_j \exp(-aI_j/I_p)$, where $0 < a \leq 1$. The modification renders H convex on $[0, 2I_p/a]$.

By minimizing H, we can obtain the minimum of the revised entropy, where I_j is exactly equal to I_p. However, the I_p is not an optimal value of I_j for an interferometric imaging system; therefore, data fidelity and total power restrictions are considered and discussed in the following section.

3.2. Revised entropy method (REM)

In the simulation, the observed data are samples of the complex visibilities of observation. They can be expressed as in Eq. (1). In the simulation, sampled visibilities correspond to a fast Fourier transform of observation I^0 and can be arranged in frequency domain with serial numbers k as follows:

$$V_k = W_k \sum_j^N w_j I_j^o \exp\left(-i2\pi \vec{f}_k \bullet \vec{x}_j\right) + n_k \tag{8}$$

where n_k represents the noise introduced by the PIIIS, and W_k is the measurement matrix of the complex visibilities. The measurement matrix contains only zero and one, corresponding to the actual baseline distribution [8]. w_j is the sample window of the observation [19], namely the FOV of PIIIS, $\vec{f}_k$ is the measured spatial frequency in the pupil plane of the kth pixel, and $\vec{x}_j$ is the position vector in the observation plane of the jth pixel. The corresponding visibility functions produced by the restoration I_j are as follows:

$$V'_k = \sum_j^N I_j \exp\left(i2\pi \vec{f}_k \cdot \vec{x}_j\right) \tag{9}$$

Moreover, additional specific equations constraining the particular imaging of PIIIS are selected to evaluate the features of revised entropy. To measure the difference of complex visibilities between the restoration and observed data, the data fidelity term is used as follows:

$$\chi^2 = \sum_k^N \left|W_k V'_k - V_k\right|^2 \tag{10}$$

Constraining only data fidelity χ^2 can lead to systematic bias in the restoration. Minimizing the revised entropy provides the benefits of suppressing high errors of deviation from the prior and acquiring least information. Moreover, minimizing data fidelity provides the benefits of suppressing the error between the sampled visibilities and the restored visibilities. However, systematic error biased by noise n_k has not been considered thus far, and this can be suppressed through minimizing the total power of the image. Therefore, we measure the total power of the restoration image as follows:

$$F = \sum_j^N I_j \tag{11}$$

Using Lagrange's undetermined multiplier method, we can restate the optimization problem as minimizing the following objective function:

$$minimum \quad J = \gamma H + \alpha\chi^2 + \beta F \tag{12}$$

$$subject\ to \begin{cases} H = -\sum_j^N I_j \exp(-I_j/I_p) \\ \chi^2 = \sum_k^N W_k \left|V'_k - V_k\right|^2 \\ F = \sum_j^N I_j \\ I_j \geq 0 \end{cases} \tag{13}$$

In the optimization problem, the modification of H can be used to stabilize the iterations, and the initial estimations of I_j are set close to

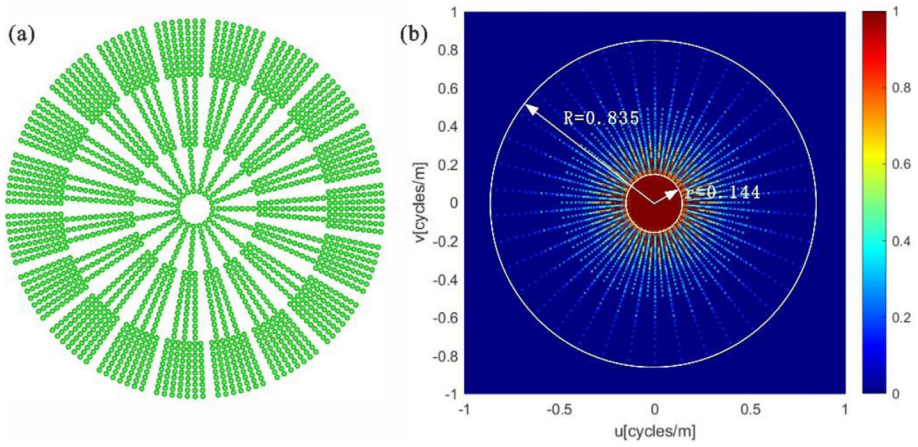

Fig. 2. (a) The hierarchical multistage sampling lens array. (b) Spatial frequency distributions of the segmented planar imaging system with 512 × 512 discrete data points of the fixed FOV.

the IFT images. Therefore, to accelerate the convergence, we adapted the Newton–Raphson method to optimize the objective function [22]. The next trial image is obtained as follows:

$$\Delta \mathrm{I} = (-\nabla\nabla \mathrm{J})^{-1} \cdot \nabla \mathrm{J} \tag{14}$$

where $\nabla \mathrm{J} = \gamma \nabla \mathrm{H} - \alpha \nabla \chi^2 - \beta \mathbf{1}$ and $\nabla\nabla \mathrm{J} = \gamma \nabla\nabla \mathrm{H} - \alpha \nabla\nabla \chi^2$. $\mathbf{1}$ represents matrix with all element equals one. Because of the low sampling rate of complex visibilities, we neglect the sidelobes of $\nabla\nabla\chi^2$. Therefore, the Hessian of the data fidelity term is a diagonal matrix, and diagonal elements can be expressed as follows:

$$\begin{aligned} \nabla_{\mathrm{j}_1} \nabla_{\mathrm{j}} \chi^2 &= \frac{\partial}{\partial \mathrm{I}_{\mathrm{j}_1}} \left(\frac{\partial \chi^2}{\partial \mathrm{I}_{\mathrm{j}}} \right) * \delta(\mathrm{j} - \mathrm{j}_1) \\ &= 2 \sum_k \mathrm{W}_{\mathrm{k}} \cos\left(\mathrm{i} 2\pi \vec{f}_k \bullet \left(\vec{x}_j - \vec{x}_{j_1} \right) \right) * \delta(\mathrm{j} - \mathrm{j}_1) \\ &= 2 \sum_{\mathrm{k}} \mathrm{W}_{\mathrm{k}} \end{aligned} \tag{15}$$

The Lagrange multipliers, α, β, and γ are adjusted during iterations to satisfy the final constraints. A simple Taylor series expansion of χ^2, F, and H helps to calculate the changes in the Lagrange multipliers [23]:

$$\begin{aligned} \Delta\alpha &= -\Delta\chi^2 / \left\| \nabla\chi^2 \cdot \nabla\chi^2 \right\| \\ \Delta\beta &= -\Delta \mathrm{F} / \left\| \nabla \mathrm{F} \cdot \nabla \mathrm{F} \right\| \\ \Delta\gamma &= -\Delta \mathrm{H} / \left\| \nabla \mathrm{H} \cdot \nabla \mathrm{H} \right\| \end{aligned} \tag{16}$$

Algorithm 1 shows the pseudocode of the REM for reconstruction.

Algorithm 1 Reconstruction algorithm using the revised entropy method

Input data W_{k}, V_{k} and w_{j}.

Calculate prior image I_{p}.

Initialize I between the zeros matrix and $\left|\mathrm{IFT}\{\mathrm{V}_{\mathrm{k}}\}\right|$, and α, β, γ.

while not converged **do**

1. Solve $\nabla \mathrm{J} = \gamma \nabla \mathrm{H} - \alpha \nabla \chi^2 - \beta \mathbf{1}$, $\nabla\nabla \mathrm{J} = \gamma \nabla\nabla \mathrm{H} - \alpha \nabla\nabla \chi^2$, and (14).
2. Update the $\mathrm{I}^{\mathrm{new}} = \mathrm{I}^{\mathrm{old}} + \Delta \mathrm{I}$ using (14).
3. Update the Lagrange multipliers α, β, and γ using (16).
4. Check convergence:

if $\left\| \mathrm{I}^{\mathrm{new}} - \mathrm{I}^{\mathrm{old}} \right\|_2 / \left\| \mathrm{I}^{\mathrm{old}} \right\|_2 <$ tolerance **then**

break

end if

end while

Table 1
System parameters used in the simulations.

Parameters	Symbols	Values
Range of wavelength	λ	380–700 nm
Object distance	z	250 km
Lenslet diameter	D	3.6 mm
Longest interferometric baseline	$B_{\max}$	104.4 mm
Number of the lenslets per column	M	30
Number of PIC	P	19
Channel number of arrayed waveguide grating	SC	16
Wavelength spacing of arrayed waveguide	$\Delta\lambda$	20 nm
Fixed FOV	f_{FOV}	$2\lambda/D$
Discrete data points of fixed FOV	N × N	512 × 512

4. Image reconstruction experiment

To illustrate the reconstruction and feasibility of suppressing the ringing artifacts using the REM, we employed a hierarchical multistage sampling lens array for our image reconstruction system architecture [6]. The lens array is composed of long, medium and short radial lenses, as shown in Fig. 2(a). The pairing method of long radial lenses is (1,30), (2,24), (3,6), (4,17), (5,7), (8,25), (9,10), (18,23), (19,29), (20,28), (21,27), (22,26), and the baseline lengths are 1, 2, 3, 4, 5, 6, 8, 10, 13, 17, 22, 29. The pairing method of medium radial lenses is (1,18), (2,4), (3,10), (5,17), (6,9), (7,8), (11,16), (12,22), (13,21), (14,20), (15,19), and the baseline lengths are 1, 2, 3, 4, 5, 6, 7, 8, 10, 12, 17. The pairing method of short radial lenses is (1,3), (2,5), (4,9), (6,10), (7,8), and the baseline lengths are 1, 2, 3, 4, 5. The spatial frequency distribution of the hierarchical multistage-sampling lens array is shown in Fig. 2(b). It had a continuous sampling radius of $r = 0.144$ and a maximum sampling radius of R = 0.835. The rest of system parameters used in the simulations are listed in Table 1.

The FOV of an interferometer using one single-mode waveguide /fiber per aperture to transport the beam is limited to $2\lambda/D$ [17]. For simplification, the FOV was set to $2\lambda/D$ and was discrete with 512 × 512 data points. Furthermore, a measurement matrix was also set to avoid visibility regridding [8].

The degraded image in the PIIIS is performed by a filter, which has a characteristic feature of the low-frequency intensive and high-frequency sparse measurement matrix in the frequency domain. This brings a sharp cut-off or truncation in the frequency domain, equivalent to a convolution in the spatial domain with a *sinc* function. Moreover, it brings a ringing pattern around sharp edges by oscillating lobes of the *sinc* function. In the PIIIS, these truncations differ with the orientations, leading to a different distance between the main lobe and the oscillating lobes of the *sinc* function. Hence, more complicated ringing artifacts arise around the object in IFT images. Moreover, these ringing artifacts

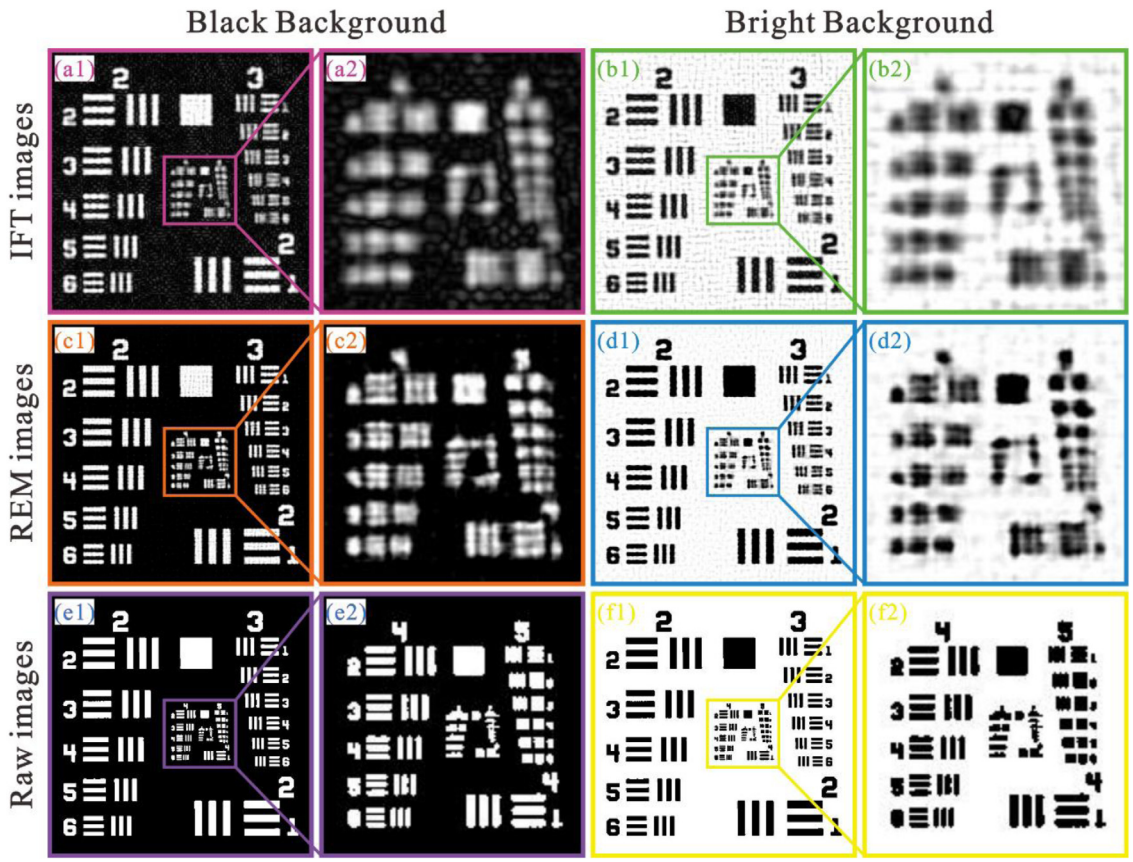

Fig. 3. Comparison of IFT, REM, and raw images for the black and bright background resolution board targets.

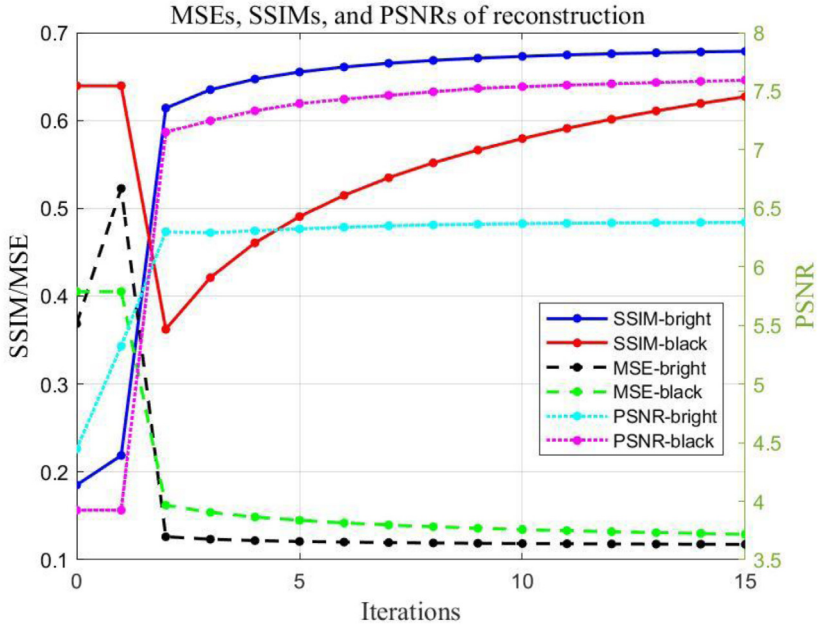

Fig. 4. MSEs, SSIMs, and PSNRs of the reconstruction results of the REM at different iterations for the bright and black background resolution board targets.

reduce the imaging quality by a large extent, which is determined by the simulation and is shown in Fig. 3 (a1), (a2), (b1), and (b2).

To quantify the effect of suppressing ringing artifacts, the similarity between the reconstructed and raw images is further evaluated using the mean squared error (MSE), peak signal-to-noise ratio (PSNR), and structural similarity (SSIM) assessments [13,24–26]. To demonstrate the ringing artifacts raised by sparse samples, we demonstrate IFT and REM reconstructions on resolution board targets with black and bright backgrounds. The IFT, REM reconstructions, and raw images of the two resolution board targets are shown in Fig. 3.

In Fig. 4 the MSEs, SSIMs, and PSNRs at different iterations are plotted over a total of 16 iterations. The indices improved rapidly

Table 2
MSE, PSNR, and SSIM reconstruction result differences for the bright and black background resolution board targets after 20 iterations.

	Methods	Assessments		
		MSE	PSNR	SSIM
Bright background target	IFT	0.0288	15.4134	0.3785
	REM	**0.0159**	**17.9724**	**0.6529**
Black background target	IFT	0.0288	15.4134	0.3784
	REM	**0.0137**	**18.6198**	**0.6803**

during the first iterations. The significant improvements in the MSE, SSIM, and PSNR after 20 iterations are shown and compared with those of IFT images in Table 2. The improvements in the MSEs, SSIMs, PSNRs, and the visual quality confirm the feasibility of suppressing the ringing effect due to the insufficient sampling of the visibility function in the PIIIS. The remaining fuzzy area in Fig. 3 (c2) and (d2) is produced by the lack of a corresponding sample of that visibility function.

5. Conclusion

Inspired by entropy, we proposed a prior-based penalty term and developed a simple algorithm using the Newton method. The prior-based penalty term was designed to penalize a high bias deviating from the ringing-free or ringing-less prior image. To retain the advantages of information entropy and stabilize the iterations, the penalty term replaced the logarithm form of the traditional entropy with a negative exponent, which led to a nonconvex revised entropy. Therefore, certain techniques were proposed to render it a convex optimization problem assuming that the optimal solution was within $[0, 2I_p/a]$ of the prior value I_p. To discuss the revised entropy penalty term, we added data fidelity to suppress the error between the sampled and restored visibilities, and the total power term was introduced to prevent systematic error biased by noise in the algorithm. In the reconstruction experiment, we adopted the hierarchical multistage sampling pattern and resolution board targets with sharp edges, which caused evident ringing effects. The resulting imaging quality and resolution were significantly improved. The revised entropy penalty showed the feasibility of suppressing ringing artifacts for PIIIS.

Declaration of competing interest

The authors declare that they have no known competing financial interests or personal relationships that could have appeared to influence the work reported in this paper.

Funding

This work was supported by National Natural Science Foundation of China (61975201) and the Youth Innovation Promotion Association of the Chinese Academy of Sciences. This work was partially supported by the Advanced Science Key Research Project, Chinese Academy of Science (QYZDJ-SSW-JSC038), and Key Foreign Cooperation Projects of International Cooperation Bureau, Chinese Academy of Science (181722KYSB20180015).

References

[1] R.L. Kendrick, et al., Flat panel space based space surveillance sensor, in: AMOS Conference, 2013.
[2] A. Glindemann, Principles of Stellar Interferometry, Springer, 2011.
[3] T. Su, et al., Interferometric imaging using Si3N4 photonic integrated circuits for a SPIDER imager, Opt. Express 26 (2018) 12801–12812, http://dx.doi.org/10.1364/OE.26.012801.
[4] T. Su, R.P. Scott, C. Ogden, S.T. Thurman, R.L. Kendrick, A. Duncan, R. Yu, S.J.B. Yoo, Experimental demonstration of interferometric imaging using photonic integrated circuits, Opt. Express 25 (2017) 12653–12665, http://dx.doi.org/10.1364/OE.25.012653.
[5] Q. Chu, et al., Numerical simulation and optimal design of segmented planar imaging detector for electro-optical reconnaissance, Opt. Commun. 405 (2017) 288–296, http://dx.doi.org/10.1016/j.optcom.2017.08.021.
[6] W.P. Gao, et al., Quantitative analysis of segmented planar imaging quality based on hierarchical multistage sampling lens array, Opt. Express 27 (2019) 7955–7967, http://dx.doi.org/10.1364/OE.27.007955.
[7] Q. Yu, et al., System design for a checkerboard imager, Appl. Opt. 57 (2018) 10218–10223, http://dx.doi.org/10.1364/AO.57.010218.
[8] C. Ding, et al., Structure design and image reconstruction of hexagonal-array photonics integrated interference imaging system, IEEE Access 8 (2020) 139396–139403, http://dx.doi.org/10.1109/ACCESS.2020.3013316.
[9] D. Krishnan, R. Fergus, Fast image deconvolution using hyper-Laplacian priors, in: Annual Conference on Neural Information Processing Systems, 2009.
[10] J. Veraart, et al., Gibbs ringing in diffusion MRI, Magn. Reson. Med. 76 (1) (2016) 301–314, http://dx.doi.org/10.1002/mrm.25866.
[11] T.B. Kai, M. Uecker, J. Frahm, Suppression of MRI truncation artifacts using total variation constrained data extrapolation, Int. J. Biomed. Imaging 2008 (2008) 184123, http://dx.doi.org/10.1155/2008/184123.
[12] E.J. Candes, M.B. Wakin, An introduction to compressive sampling, IEEE Signal Process. Mag. 25 (2008) 21–30, http://dx.doi.org/10.1109/MSP.2007.914731.
[13] X. Zhao, et al., Gibbs-ringing artifact suppression with knowledge transfer from natural images to MR images, Multimedia Tools Appl. 79 (2020) 33711–33733, http://dx.doi.org/10.1007/s11042-019-08143-6.
[14] H.S. Kong, et al., Coding artifacts reduction using edge map guided adaptive and fuzzy filtering, in: IEEE International Conference on Multimedia & Expo, 2005.
[15] R. Archibald, A. Gelb, A method to reduce the Gibbs ringing artifact in MRI scans while keeping tissue boundary integrity, IEEE Trans. Med. Imaging 21 (2002) 305–319, http://dx.doi.org/10.1109/TMI.2002.1000255.
[16] E. Thiébaut, J.-F. Giovannelli, Image reconstruction in optical interferometry, IEEE Signal Process. Mag. 27 (2011) 97–109, http://dx.doi.org/10.1109/MSP.2009.934870.
[17] Q. Yu, D. Wu, F. Chen, S. Sun, Design of a wide-field target detection and tracking system using the segmented planar imaging detector for electro-optical reconnaissance, Chin. Opt. Lett. 16 (2018) 071101.
[18] M. Cárcamo, et al., Multi-GPU maximum entropy image synthesis for radio astronomy, Astron. Comput. 22 (2018) 16–27, http://dx.doi.org/10.1016/j.ascom.2017.11.003.
[19] N. Wu, The Maximum Entropy Method, Springer, 1997.
[20] P. Rodríguez, B. Wohlberg, Efficient minimization method for a generalized total variation functional, IEEE Trans. Image Process. 18 (2009) 322–332, http://dx.doi.org/10.1109/TIP.2008.2008420.
[21] J.W. Goodman, Introduction to Fourier Optics, third ed., Robert and Company, Colorado, 2004.
[22] S. Boyd, L. Vandenberghe, Convex Optimization, Cambridge University Press, 2004, http://dx.doi.org/10.1017/CBO9780511804441.
[23] T. Cornwell, K.F. Evans, A simple maximum entropy deconvolution algorithm, Astron. Astrophys. 143 (1985) 77–83, http://dx.doi.org/10.1086/131942.
[24] Z. Wang, A.C. Bovik, H.R. Sheikh, E.P. Simoncelli, Image quality assessment: From error visibility to structural similarity, IEEE Trans. Image Process. 13 (2004) 600–612, http://dx.doi.org/10.1109/TIP.2003.819861.
[25] A.M. Tekalp, M.I. Sezan, Quantitative analysis of artifacts in linear space-invariant image restoration, Multidimens. Syst. Signal Process. 1 (1990) 143–177, http://dx.doi.org/10.1007/BF01816547.
[26] R. Liu, J. Jia, Reducing boundary artifacts in image deconvolution, in: 2008 15th IEEE International Conference on Image Processing, IEEE, 2008.